An Electrode Extension Model for Gas Metal Arc Welding

Short circuiting transfer can be predicted within 9% for a given electrode feed speed

BY T. P. QUINN, R. B. MADIGAN AND T. A. SIEWERT

ABSTRACT. The electrode extension during gas metal arc welding is predicted using a one-dimensional model of the melting electrode. Joule heating in the electrode, heat directly applied to the end of the electrode from the condensing electrons, and heat transferred from the droplet, together with conduction along the electrode are considered. The thermal conductivity, the thermal diffusivity, and the electrical resistivity of the electrode material are allowed to vary with temperature. The steady-state electrode extension is predicted to an accuracy of 1.9 mm (0.074 in.). The onset of short-circuiting as the current is decreased for a given electrode feed speed is predicted within 9%. Dynamic analysis shows that the gas metal arc welding process acts as a low-pass filter for electrode extension with respect to the square of the current (proportional to power) and with respect to electrode feed speed. As the mean welding current is increased, the electrode extension (or arc length if the contact-tube-to-work distance is constant) has a smaller response to perturbations in the current or electrode feed speed. The quasi-linear transfer functions between electrode extension and current squared and between electrode extension and electrode feed speed can be described by one zero, two pole parametric fits. The transfer functions are linear in the amplitude of the excitation up to 10% of the mean excitation. The model transfer functions were verified with experiments.

T. P. QUINN, R. B. MADIGAN and T. A. SIEWERT are with National Institute of Standards and Technology Boulder, Colo.

Introduction

This paper presents a model for electrode extension during gas metal arc welding (GMAW). In GMAW, an arc is created between the continuously fed, consumable electrode and the workpiece. The melted electrode acts as filler metal in the weld. The length of the solid electrode from the point of current transfer to where the electrode is melted, the electrode extension (EE) determines the length of the arc and, therefore, the amount of power used in the welding process. Transfer mode (globular, spray, etc.), arc stability, and deposition rate depend on the EE (Ref. 1).

The way in which the metal is transferred from the electrode to the weld pool affects the final shape and quality of the weld (Ref. 1). Spray transfer (when the diameters of the detached droplets are equal to or smaller than the electrode diameter) is the highest production transfer mode. Short circuit transfer (when the electrode comes into direct electrical contact with the workpiece) is often used for thin or heat-sensitive materials (Ref. 1). It is desirable to be able to predict the transfer mode from the process variables both for automatic control and for weld schedule design.

KEY WORDS

Electrode Extension
GMAW
One-dimension Model
Temperature Profile
Describing Function
Spray Transfer Mode
Welding Current
Electrode Feed Speed
Transfer Functions
Stefan Problem

Halmoy (Refs. 2–4) neglected thermal conduction and used an energy balance at the tip of the electrode to calculate the steady state (Ref. 2) and dynamic melting rates (Ref. 4), as well as the EE. He assumed a fixed EE and heat generation from the arc and Joule heating. Waszink and van den Heuvel (Ref. 5) assumed a fixed EE and included the effects of conduction, the Thomson effect, radiation, and Joule heating. They found the losses from radiative heat transfer and the Thomson effect to be about two orders of magnitude less than the contributions of Joule heating and heat from the arc. Conductive heat transfer was larger than or of the same order of magnitude as Joule heating in about the first 25% of the electrode from the contact point. The heat conducted from the liquid at the electrode tip was 33% of the total Joule heating at 137 A and 11% of the total Joule heating at 238 A for the 1.2-mm (0.045-in.) steel electrode they studied. Data for the EE, current and electrode feed speed or wire feed speed were experimentally determined.

Kim, *et al.* (Ref. 6), concluded that an energy balance approach was "inadequate to explain the observed melting phenomena." Using a steady state, two-dimensional model with conduction, he predicted the temperature distribution in the electrode. Again, EE, current and electrode feed speed were determined experimentally. He modeled the heat transferred to the melting tip of the solid

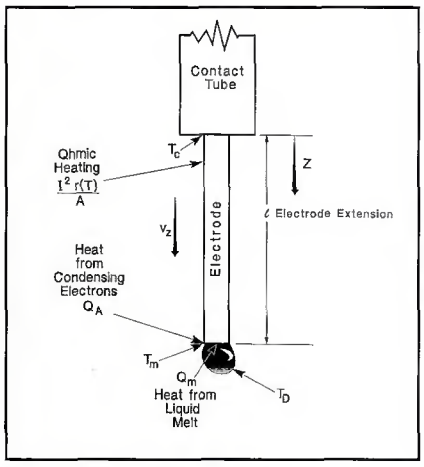

Fig. 1 — The melting electrode model.

electrode as coming from two sources: heat transferred from the liquid, and heat directly delivered to the solid electrode by the arc.

There has been no attempt known to the authors to predict EE from the process variables (current, electrode feed speed, electrode composition, and electrode diameter) using a model that includes conduction.

Dynamic models of GMAW are needed to facilitate control of the process. Wu and Richardson (Ref. 7) used Halmoy's model of the electrode (Ref. 4) in an overall dynamic model of the entire GMAW process. Kannatey-Asibu (Ref. 8) used an experimentally identified first-order equation to model the dynamics of the arc length where EE plus arc length is equal to the contact-tube-to-work distance (CTWD).

The purposes of this research were: 1) develop a dynamic and steady-state model that predicts EE for GMAW from the other process variables; 2) determine the steady-state process variables at which short circuit transfer takes place; and 3) quasi-linearize the model to a set of transfer functions for use in automatic control. A thermal conduction model that includes heat sources from Joule heating, heat from electrons that condense directly on the solid electrode, and heat transferred from the liquid drop at the electrode tip was developed for the spray transfer mode. The resulting set of partial differential equations (a one-phase Stefan problem) was solved for the transient and steady-state cases. Quasi-linear transfer functions (using the method of describing functions (Ref. 9) between EE and the square of the current and EE and electrode feed speed were developed. The transfer functions describe the dynamic relationship between the input, current squared or electrode feed speed, and the output, EE.

Table 1 — Optimal Material Constants and γ for E100S-1 and Nominal Material Constants for Fe (Refs. 12–15). The Nominal Values for Fe Were Used Except Where Noted

	Fe	E100S-1
$\alpha(T_m)$, m^2/s	6.30×10^{-6}	6.93×10^{-6}
$K(T_m)$, W/(m·K)	34.6	31.1
$r(T_m)$, μΩ·m	1.32	1.52
L, J/kg	2.72×10^5	—
T_m, °C	1510	—
$c(T_m)$, J/(kg·K)	751	—
V_c, V	6.00	—
γ	—	0.08

Model

Neglecting heat losses due to the Thomson effect and radiation, the one-dimensional governing equation for the rate of heat transfer in the electrode is

$$\frac{\partial}{\partial Z}\left(K(T)\frac{\partial T}{\partial Z}\right)+\frac{I^2(t)r(T)}{A^2}=\left(v_Z(t)\frac{\partial T}{\partial Z}+\frac{\partial T}{\partial t}\right)c(T)\rho(T) \tag{1}$$

(see Fig. 1). Here, T is temperature; K is thermal conductivity; I is current; r is resistivity; A is the cross-sectional area; v_z is electrode feed speed, c is specific heat and ρ is the density. The boundary conditions are

$$T(Z=0)=T_c,$$
$$T(Z=\ell(t))=T_m \tag{2}$$

where T_c is the temperature of the contact tube and T_m is the melting temperature. An additional condition is necessary because the boundary moves with time:

$$-K(T)\frac{\partial T}{\partial Z}+\frac{Q_A(t)}{A}+\frac{Q_m(t)}{A}=\rho(T)L\left(v_Z(t)-\frac{d\ell}{dt}\right) \tag{3}$$

(the energy balance at the tip of the solid electrode). Here, Q_A is the rate of heat transfer to the solid electrode from condensing electrons ($z=\ell$). Q_m is the rate of heat transfer from the liquid melt. This set of equations with the addition of the initial conditions,

$$\ell(t=0)=\ell_o,$$
$$T(Z,t=0)=T_o(Z) \tag{4}$$

is a one-phase Stefan problem (Ref. 10).

Following the developments of Kim (Ref. 11), a percentage of the condensation heat is applied directly to the solid electrode at $z = \ell$ giving

$$Q_A=\gamma V_c I \tag{5}$$

where V_c is the apparent condensation voltage and γ is the fraction of electrons that condense on the solid electrode. As shown in the appendix, the rate of heat transferred from the melt can be approximated by

$$Q_m=\frac{V_c(1-\gamma)I}{2}. \tag{6}$$

γ must be determined experimentally. As seen in the appendix, the equations are first nondimensionalized and then solved using a finite difference method. The equations governing steady-state heat transfer and their method of solution are also shown in the appendix.

There is a lack of data across the temperature range of interest (room temperature to melting point) for the thermal diffusivity α(T), electrical resistivity r(T) and thermal conductivity K(T) for the low-carbon steel electrode (E100S-1) used in the experiments; γ is also unknown. To approximate the material properties, the data for pure Fe (Refs. 13–15) are used and corrected for the material used in the experiments. (For pure Fe, the data at the melting point have an estimated uncertainty of ±20%, so a similar procedure would be required even if a pure Fe electrode were used.) The data for Fe are multiplied by a constant over the temperature range. To find the multiplication constants for the material properties and to find γ, the error between the experimental steady-state EE ℓ_{ss} and the model ℓ_{ss} minimized as the constants are varied. Grid searches ranging ±15% around the nominal values of Fe with 5% steps are used to find $\alpha(T_m)$, $r(T_m)$, $K(T_m)$. γ was varied between 0.05 and 0.25 in 0.005 steps.

To understand the dynamics of the system around the steady-state solutions, the method of describing functions (Ref. 9) is used. Approximate transfer functions between the dimensionless EE $s(t) = \ell/\ell_o$ and the dimensionless, volumetric Joule heat generation

$$q_j(t)=\frac{I^2(t)\ell_0^2 r(T_m)}{A^2K(T_m)(T_m-T_c)}$$

and between s and the Peclet number

$$W(t)=\frac{\ell_0 v_Z(t)}{\alpha(T_m)}$$

are calculated. W and q_j are varied about their steady-state values W_{ss} and q_{jss}:

$$q_j=q_{jss}+a_{qj}\sin(2\pi\omega\tau)$$
$$W=W_{ss}+a_w\sin(2\pi\omega\tau) \tag{7}$$

where a_{qj} and a_w are the amplitudes of the oscillations.

$$\tau = \frac{t\alpha(T_m)}{\ell_0^2}$$

is the Fourier number, and ω is the dimensionless frequency of oscillation. The response of s in τ is then calculated using the temperature distribution of the steady-state solution as the initial condition. To calculate the magnitude and phase of the transfer function at ω, a and ψ are found in

$$s = a\ sin(\omega\tau + \psi) \tag{8}$$

through a least squares fit. The magnitude of the transfer function at ω is then predicted to be a/a_{qj}. The phase of the transfer function is predicted by ψ. Once transfer function data at discrete frequencies are determined, parametric, rational curves are fitted to the transfer functions according to the procedure of Lin and Wu (Ref. 16).

Experiments

Bead-on-plate welds were made with a 1.14 mm (0.045 in.) E100S-1 electrode, 15–22 mm (0.6–0.9 in.) CTWD, and 95% Ar-5% CO_2 gas. A low-noise regulator was used as described in Ref. 17 to maintain constant current. To obtain EE measurements, a 10 mW He-Ne laser and 632-nm bandpass filter were used to create a shadowgraph of the electrode and base plate (Ref. 17). The shadowgraph images were recorded on a high-speed video system. The contact tube, the electrode, and the workpiece were imaged.

The current was measured with a Hall effect transducer with an absolute error of 1%. The voltage between the torch and the baseplate was measured within 0.5% absolute error. The axial velocity of the electrode or feed speed (v_z) was measured as the electrode entered the wire feeder. A pinch roller (16 mm diameter) was attached to an optical encoder (5000 pulses/rev) and the resulting pulse train was frequency converted to give a voltage signal proportional to v_z. The rms uncertainty from calibration tests for the transducer was 2 mm/s.

Experiments were undertaken to develop and verify the model for steady-state conditions. The welding current, welding voltage and v_z signals were low-pass filtered with a cutoff frequency of 3000 Hz and recorded on a laboratory computer at 8928 samples/s. The video data were recorded at 3000 frames/s with 0.2 mm/pixel resolution. The data were recorded for about 2 s during welding.

Experiments were also conducted under dynamic conditions to verify the model. The I^2 or v_z was varied sinusoidally about a mean value at selected frequencies; v_z or I, respectively, was maintained constant. The data recording rates were reduced because of the relatively long data recording period (~30 s). Here, the voltage, v_z, and current were sampled at 210 samples/s after being low-pass filtered with a cutoff frequency of 100 Hz. The video data were recorded at 250 frames/s.

The end of the solid electrode was defined as the point midway between where the electrode starts to neck (spray transfer) and where droplets formed. The point of current transfer was assumed to be at the exit of the contact tube. The EE was determined from the video data by counting the number of pixels between the contact tube and electrode end frame by frame. For the dynamic experiments the EE was measured automatically to within about 0.9 mm by capturing the video data frame by frame and detecting the outline of the electrode using an image processor.

The phase and amplitude of the current squared or electrode feed speed and the EE in the dynamic experiments were determined by least-squares fitting the data with a sine wave. The EE to current or EE to electrode feed speed transfer function were then constructed by taking the ratio of the magnitudes $||\ell/I^2||$ or $||\ell/v_z||$ and taking the difference in the phases $\angle\ell - \angle I^2$ or $\angle\ell - \angle v_z$.

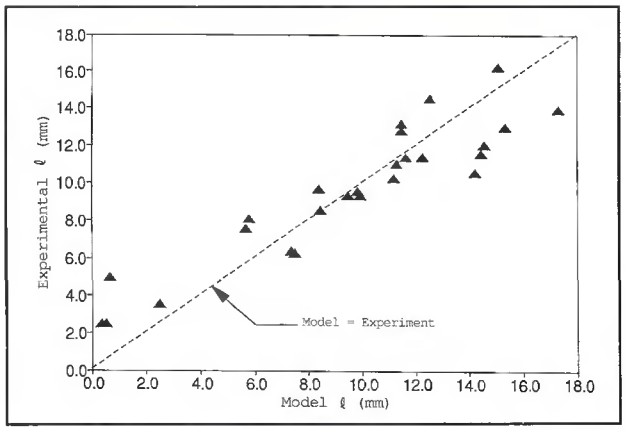

Fig. 2 — Model electrode extension calculated using the parameters in Table 1 and the experimental electrode extension.

Result

Using the optimal material constants and the optimal γ (Table 1), the standard deviation between the steady-state EE measured in the experiments and the steady-state EE predicted by the model is 1.9 mm for the E100S-1 electrode — Fig. 2. The steady-state model EE is derived from the relationship between $q_{j\,ss}$ and W_{ss} — Fig. 3.

Figure 3 can also be used to determine a lower bound on the current at which short circuiting will occur. By assigning ℓ_0 = CTWD and using the optimal material properties in Table 1, Fig. 3 can be transformed to a relationship between current and v_z. Short circuiting will actually occur at currents higher than those predicted because droplets will bridge between the electrode tip and the weld pool; the current predicted here is that which would cause the electrode to enter the weld pool. Using the data in Ref. 17, the predicted short circuiting is compared to the actual onset of short circuiting — Fig. 4. The largest difference between the predicted and measured currents at the onset of short circuiting is 9% at 187 mm/s (442 in./min).

For large W such as are produced when v_z or ℓ_0 is large, the model predicts a steady-state temperature distribution

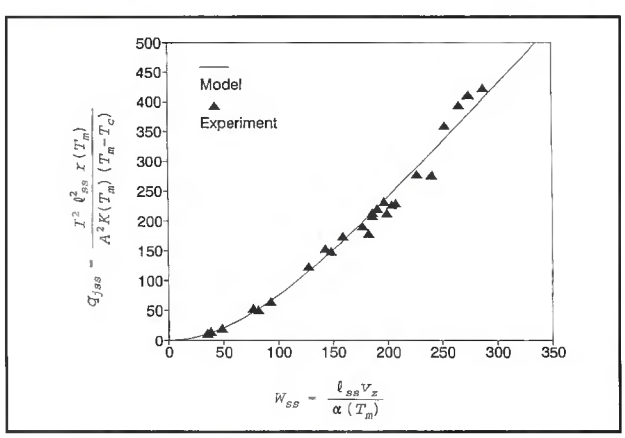

Fig. 3 — Model $q_{j\,ss}$ calculated using the parameters of Table 1 and the experimental results.

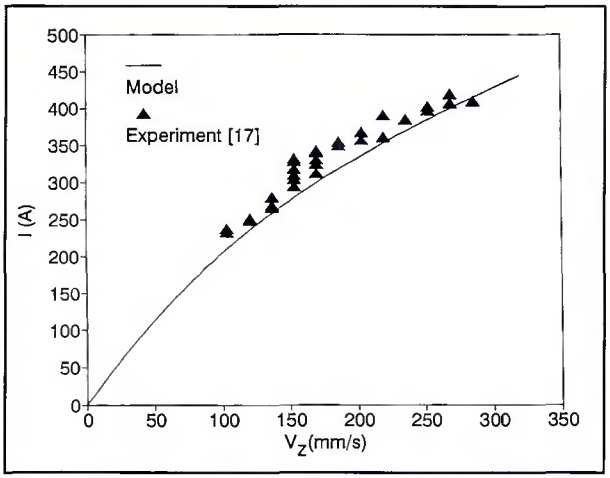

Fig. 4 — The model-predicted onset of short circuiting transfer as the welding current is decreased, calculated using the parameters of Table 1 and the experimental results. The CTWD was 13 mm.

$$u = \frac{T - T_c}{T_m - T_c}$$

which is nearly linear in $x = Z/\ell_0$ until a point near the melting boundary is reached where there is a sharp rise in u — Fig. 5. For example, when W = 300.5, u = 0.238 x for $0 \le x \le 0.98$ with a correlation coefficient of 0.998; 75% of the increase in u occurs in the last 2% of the electrode. For small W, u rises more gradually; when W = 0.5, 75% of the increase in u occurs in the last 23% of the electrode — Fig. 5.

The dynamic response of EE to sinusoidal excitation in I^2 and v_z shows a single frequency response at the frequency of the excitation (nonlinear systems can show response at frequencies other than the excitation frequency). The response of the EE is characterized by the transfer functions (Figs. 6, 7), which show that the process acts as a low-pass filter for EE with respect to I^2 and v_z. The magnitude of the transfer functions in s/q_j and s/W are essentially flat with increasing ω until the cutoff frequency is reached, after which the magnitude decreases one order of magnitude for a one-decade increase in ω. The magnitude decreases with increasing W but the cutoff frequency increases with increasing W. For example, for W = 75, $||s/q|| = 0.16$ until $\omega = 0.35$ where it begins to roll off; for W = 425, $||s/q|| = 0.20$ until $W \doteq 20$ where it begins to roll off. For s/q_j (or s/W), the phase starts near 180 deg (0 deg for s/W) for $\omega << 1$, passes through 90 deg (–90 deg for s/W), and returns above 90 deg (–90 deg for s/W) as ω increases.

The model prediction for ℓ/I^2 was compared to experiment for v_z = 0.12 m/s and sinusoidal oscillations in I^2 of amplitude 7 to 10% of the mean I^2 = 62500 A^2 (I = 250 A) — Fig. 8. The rms differences between the model prediction and the experiment were 0.6×10^{-7} m/A^2 in magnitude and 11 deg in phase; the model prediction is reasonably close to the experimental results. The model prediction for ℓ/v_z was compared to experiment for I = 250 A and sinusoidal oscillations in v_z of 10% of the mean 0.12 m/s. The model again closely predicts the experimental results; the rms differences between the model prediction and the experiment were 0.04 s^{-1} in magnitude and 8 deg in phase.

The least squares parametric fits of the transfer functions s/q_j and s/W (Figs. 6, 7) were two pole, one zero models of the form

$$\frac{b_0 + b_1\sigma}{1 + a_1\sigma + a_2\sigma^2}$$

where σ is the Laplace variable. For s/q_j at W = 75 and for s/W at mean W < 175, the best fitting rational function, according to the criteria of Lin and Wu (Ref. 16), is a one pole, no zero model ($b_1 \equiv 0$, $a_2 \equiv 0$). For s/q_j and s/W, a_1 and a_2 decrease with increasing mean W — Figs. 10, 11. For s/q_j, b_0 and b_1 increase with increasing W (Fig. 12), but for s/W, b_0 and b_1 decrease with increasing mean W — Fig. 13.

The transfer functions magnitude and phase for s/q_j and s/W were nearly independent of the excitation amplitude for $a_{qj} \le 0.10 q_{j\,ss}$ and $a_w \le 0.10\ W_{ss}$. For s/q_j, the identified parametric coefficients with $a_{qj} = 0.075 q_{j\,ss}$ were within (4×10^{-4}, 5×10^{-6}, 8×10^{-4}, 3×10^{-6}) of the (a_1, a_2, b_0, b_1) with $a_{qj} = 0.10 q_{j\,ss}$ — Figs. 10, 12. For s/W, the identified parametric coefficients with $a_w = 0.075 W_{ss}$ were within (6×10^{-3}, 2×10^{-6}, 2×10^{-2}, 3×10^{-6}) of the (a_1, a_2, b_0, b_1) with $a_w = 0.10 W_{ss}$ — Figs. 11, 13. Since

$$q_j = \frac{I^2(\tau)\ell_0^2 r(T_m)}{A^2 K(T_m)(T_m - T_c)}$$

a 10% perturbation in q_j corresponds to a 32% perturbation in I.

Discussion

The value of γ found here, 0.08, is near that predicted by Kim, *et al.* (Ref. 6), of $0.1 \le \gamma \le 0.25$ for spray transfer. The optimal values for $\alpha(T_m)$, $r(T_m)$, and $K(T_m)$ lie within 15% of the nominal values for pure Fe, as would be expected for the low-alloy steel E100S-1 used in the experiments. There is a 20% uncertainty in these material constants for Fe itself. Even if $\alpha(T_m)$, $r(T_m)$, and $K(T_m)$ for the electrode were known, the steady-state experiments would need to be conducted to determine γ. The prediction of the current at the onset of short circuiting within 9% offers an independent confirmation of the model as does the data for the transfer function seen in Figs. 8 and 9. The (small) differences between the model transfer functions and those found experimentally (rms differences of 0.6×10^{-7} m/A^2 in magnitude and 11 deg in phase for ℓ/I^2 and 0.04 s^{-1} in magnitude and 8 deg in phase for ℓ/v_z indicate that the model can be used to design and implement a control system for EE.

Dynamic analysis of the EE shows that the EE, and hence arc length, becomes more stable as the mean current (q_j) increases — the EE is less affected by perturbations in the current or wire feed speed.

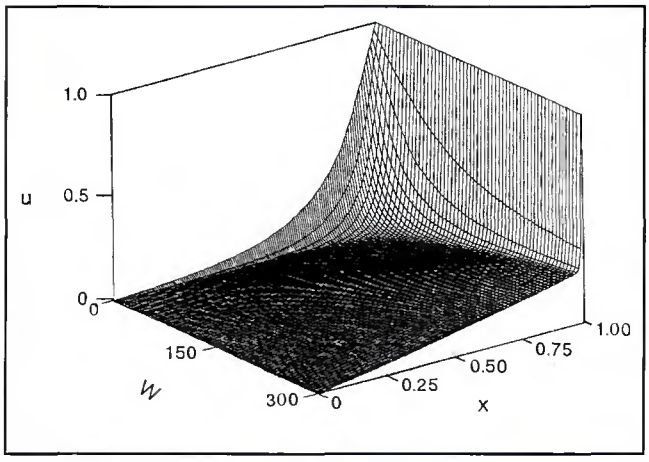

Fig. 5 — Model temperature distribution where $u = \frac{T - T_c}{T_m - T_c}$, $W(t) = \frac{\ell_0 v_z(t)}{\alpha(T_m)}$, *and* $x = Z/\ell_0$.

Conclusions

1) A dynamic and steady-state model that predicts electrode extension in the spray transfer mode of gas metal arc welding has been developed. The model predicted the steady-state electrode extension within 1.9 mm and the current at the onset of short circuiting within 9% for an E100S-1 electrode.

2) Dynamic analysis using the method of describing functions shows that as the welding current is increased, the electrode extension (or arc length if the contact-tube-to-work distance is constant) becomes more stable. Gas metal arc welding acts as a low-pass filter for electrode extension with respect to the square of the current (proportional to power) and with respect to the electrode feed speed.

3) The quasi-linear transfer functions between electrode extension and current squared and between electrode extension and electrode feed speed can be described by one zero, two pole parametric fits.

4) The transfer functions between the electrode extension and the current squared are linear in the amplitude of the current squared excitation up to 10% of the mean current squared. The transfer functions between the electrode extension and the electrode feed speed are also linear in the amplitude of the electrode feed speed excitation up to 10% of the mean electrode feed speed.

5) The dynamic response of the model was verified by experiments: at a mean current of 250 A and a mean electrode feed speed of 0.12 m/s, the model transfer function between electrode extension and current squared was within 0.6 x 10^{-7} m/A^2 in magnitude and 11deg in phase of the experimental results between 0.1 and 2 Hz. The model transfer function between electrode extension and electrode feed speed was within 0.04 s^{-1} in magnitude and 8 deg in phase of the experimental results.

References

1. American Welding Society, 1991. *Welding Handbook*, Vol. 2, pp. 109–113, Miami, Fla.

2. Halmoy, E. May 1979. Wire melting rate, droplet temperature, and effective anode melting potential. *Int. Conf. Arc Physics and Weld Pool Behavior*, The Welding Institute, London, England.

3. Halmoy, E. 1986. Electrode wire heating in terms of welding parameters. *The Physics of Welding*, ed. J. F. Lancaster, pp. 330–336, Oxford, Pergamon Press.

4. Halmoy, E., and Broten, H. 1979. Dynamic response of the wire melting rate. *Public Session Bratislava*, pp. 54–61, International Institute of Welding.

5. Waszink, J. H., and van den Heuvel, G. J. 1979. Measurements and calculations of

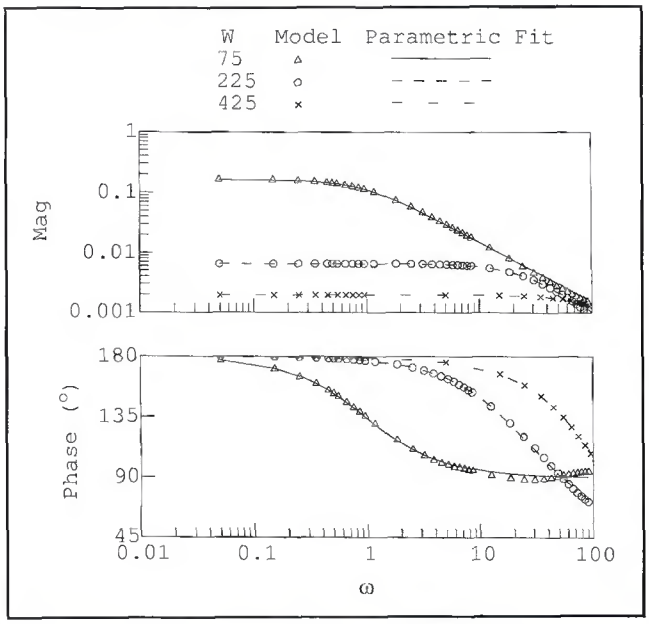

Fig. 6 — The transfer functions of s/q_j where $mag = \left\|\frac{\ell}{I^2}\right\| \frac{A^2 K(T_m)(T_m - T_c)}{\mathcal{V}_0^3 r(T_m)}$, phase $= \angle\ell - \angle I^2$, and $\omega = \frac{\ell_0^2}{\alpha(T_m)} f$; f is the frequency. $W = \frac{\ell_0 v_z}{a(T_m)}$.

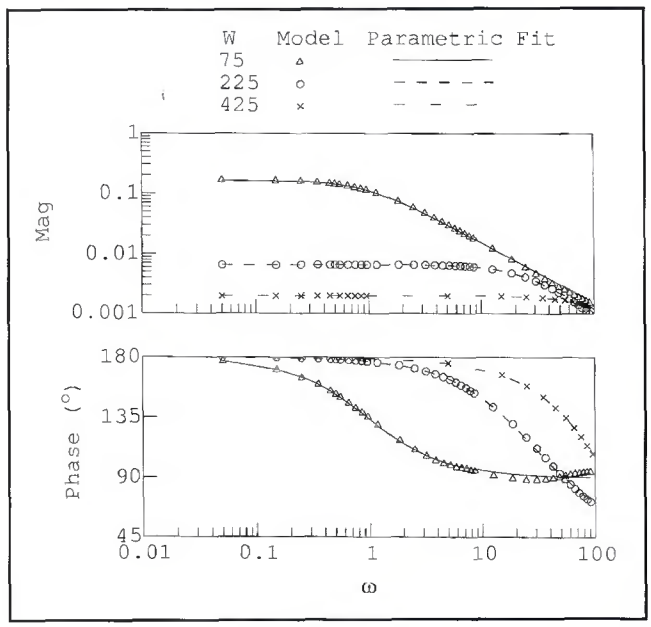

Fig. 7 — The transfer functions of s/W where $mag = \left\|\frac{\ell}{v_z}\right\| \frac{\alpha(T_m)}{\ell_0^2}$, phase $= \angle\ell - \angle v_z$, and $\omega = \frac{\ell_0^2}{\alpha(T_m)} f$; f is the frequency $W = \frac{\ell_0 v_z}{\alpha(T_m)}$.

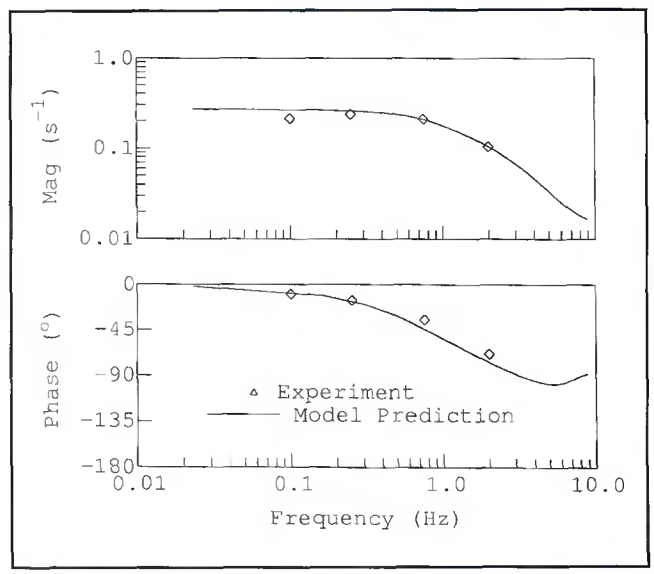

Fig. 8 — Model transfer function ℓ/I^2 calculated using the values in Table 1 for v_Z = 0.12 m/s and the mean I = 250 A and the experimental results.

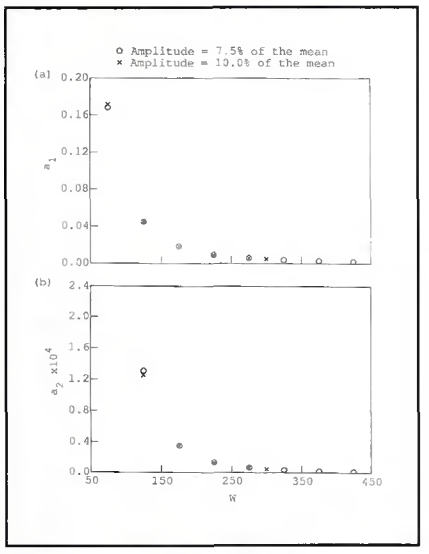

Fig. 9 — Model transfer function calculated using the values in Table 1 for a mean v_Z = 0.12 m/s and I = 250 A and the experimental results.

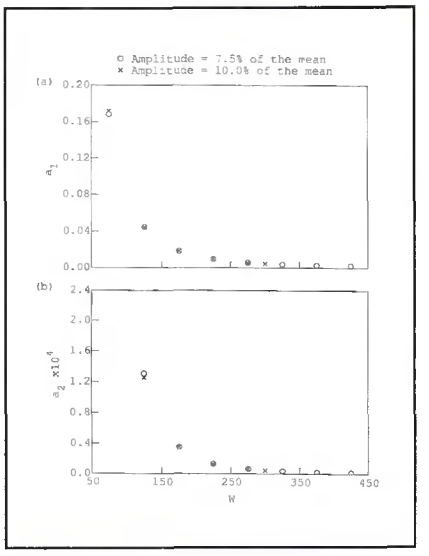

Fig. 10 — The coefficients in the denominator of parametric fits to the model transfer function

$$\frac{s}{q_j} = \frac{\ell}{I^2} \cdot \frac{A^2 K(T_m)(T_m - T_c)}{t_0^3 r(T_m)}, \text{ as a function of } W = \frac{\ell_0 v_z}{\alpha(T_m)}.$$

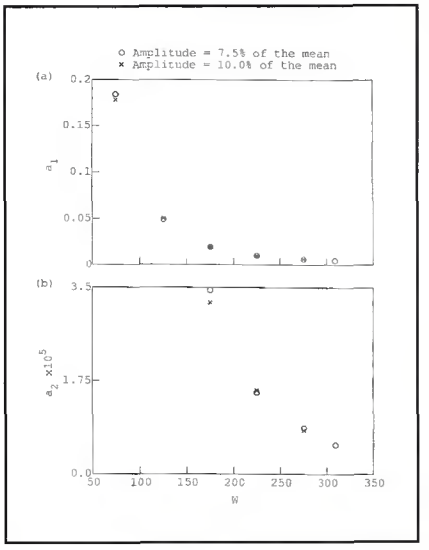

Fig. 11 — The coefficients in the denominator of parametric fits to the model transfer function

$$\frac{s}{W} = \frac{\ell}{v_z} \cdot \frac{\alpha(T_m)}{\ell_0^2}, \text{ as a function of } W = \frac{\ell_0 v_z}{\alpha(T_m)}.$$

the resistance of wire extension in arc welding. *Int. Conf. Arc Physics and Weld Pool Behavior,* pp. 227–239, The Welding Institute, London, England.

6. Kim, Y.-S., McEligot, D. M., and Eagar, T. W. 1991. Analyses of electrode heat transfer in gas metal arc welding. *Welding Journal,* 70(1): 20-s to 31-s.

7. Wu, G.-D., and Richardson, R. W. 1989. The dynamic response of self-regulation of the welding arc. *Recent Trends in Welding Science and Technology,* pp. 929–931, ASM International, Materials Park, Ohio.

8. Kannatey-Asibu, E., Jr. 1987. Analysis of the GMAW process for microprocessor control of arc length. *Journal of Engineering for Industry,* Vol. 109, pp. 172–176.

9. Leigh, J. R. 1983. *Essentials of Nonlinear Control Theory,* Topics in Control, pp. 10–22, IEEE.

10. Crank, J. 1984, *Free and Moving Boundary Problems,* Oxford University Press, Oxford, England.

11. Kim, Y.-S. 1982. *Metal Transfer in Gas Metal Arc Welding,* Ph.D. Thesis, Massachusetts Institute of Technology.

12. Touloukian, Y. S. 1967 The elements. *Thermophysical Properties of High Temperature Solid Materials,* 1, pp. 7–581, MacMillan Co., New York, N.Y.

13. Touloukian, Y. S., Powell, R. W., Ho, C. Y., and Nicolaou, M. C. 1973. Thermal diffusivity. *Thermophysical Properties of High Temperature Solid Materials,* 10, pp. 2–82, IFI/Plenum, N.Y.

14. Touloukian, Y. S., and Buyco, E. H. 1970. *Specific Heat.* Thermophysical properties of high temperature solid materials, 4, pp. 1–102, IFI/Plenum, N.Y.

15. Touloukian, Y. S., Powell, R. W., Ho, C. Y., and Klemens, P. G. 1970. Thermal conductivity. *Thermophysical Properties of High Temperature Solid Materials,* 1, pp. 9–109, IFI/Plenum, N.Y.

16. Lin, P. L., and Wu, Y. C. 1982. Identification of multi-input multi-output linear systems from frequency response data. *Journal of Dynamic Systems, Measurement, and Control,* Vol. 104, pp. 58–64.

17. Heald, P. R., Madigan, R. B., Siewert, T. A., and Liu, S. 1991. Droplet transfer modes for a MIL 100S-1 GMAW electrode. NISTIR 3976, Gaithersburg, Md., NIST.

18. Press, W. H., Flannery, B. P., Teukolsky, S. A., and Vetterling, W. T. 1988. *Numerical Recipes in C,* pp. 601–621, Cambridge University Press, Cambridge, England.

19. Forsythe, G. E., and Wasow, W. R. 1960. *Finite-Difference Methods for Partial Differential Equations,* pp. 68–71, John Wiley and Sons, New York, N.Y.

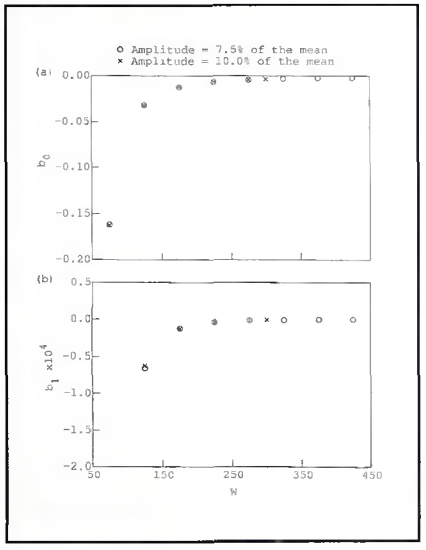

Fig. 12 — The coefficients in the numerator of parametric fits to the model transfer function

$$\frac{s}{q_j} = \frac{\ell}{I^2} \cdot \frac{A^2 K(T_m)(T_m - T_c)}{t_0^3 r(T_m)}, \text{ as a function of } W = \frac{\ell_0 v_z}{\alpha(T_m)}.$$

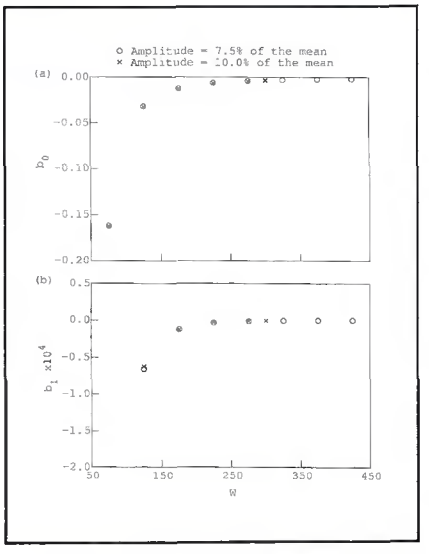

Fig. 13 — The coefficients in the numerator of parametric fits to the model transfer function

$$\frac{s}{W} = \frac{\ell}{v_z} \cdot \frac{\alpha(T_m)}{\ell_0^2}, \text{ as a function of } W = \frac{\ell_0 v_z}{\alpha(T_m)}.$$

Nomenclature

a	Amplitude of response in s
a_1, a_2, b_0, b_1	Coefficients in fit of transfer functions
a_{qj}, a_w	Amplitude of sinusoidal excitation in q_j or W.

A — Cross-sectional area of the electrode

c(T) — Specific heat

$C(u) = 1/\alpha\left(u[T_m - T_c] + T_c\right)$ — Reciprocal of thermal diffusivity

e — Electron charge

$F = \dfrac{V_c^2\left(\dfrac{\gamma+1}{2}\right)^2}{K(T_m)r(T_m)(T_m - T_c)}$ — Multiplying factor used for convenience

I(t) — Welding current

J_D — Current density in the drop

k — Boltzmann's constant

K(T) — Thermal conductivity

ℓ — Electrode extension — Fig. 1

L — Latent heat

$q_j(t) = \dfrac{I^2(t)\ell_0^2 r(T_m)}{A^2 K(T_m)(T_m - T_c)}$ — Dimensionless, volumetric, heat generation

$Q_A(T)$ — Rate of heat transfer to solid electrode from condensing electrons (z = ℓ)

$Q_m(T)$ — Rate of heat transfer to solid electrode from the melt (z = ℓ)

r(T) — Resistivity of electrode

r_D — Resistivity of the liquid in the drop

$r^*(u) = \dfrac{r\left(u[T_m - T_c] + T_c\right)}{r(T_m)}$ — Dimensionless resistivity

$s(t) = \ell(t)/l_0$ — Dimensionless electrode extension

t — Time

t_D — Period of droplet detachment

T — Temperature of electrode; subscripts c and m refer to T at z = 0(contact tip) and z = ℓ (melting). Subscripts e and D refer to the temperature of the condensing electrons and the temperature of the drop.

$u = \dfrac{T - T_c}{T_m - T_c}$ — Dimensionless temperature

$v = \int_o^u K\left(\zeta \cdot [T_m - T_c] + T_c\right) d\zeta$ — Transformed temperature

V_m — V at u = 1 (melting)

V_z — Wire feed speed

V_a — Anode fall

V_c — Apparent condensation voltage

V_D — Volume of the drop

$W(t) = \dfrac{\ell_0 V_z(t)}{\alpha(T_m)}$ — Peclet Number

$x = Z/\ell_0$ — Dimensionless coordinate

Z — Spatial coordinate — Fig. 1

Subscripts

0 — Refers to the variable at t = 0

ss — Refers to the variable at the steady-state solution

Greek

$\alpha(T)$ — Thermal diffusivity = $\dfrac{K'}{\rho c}$

γ — Fraction of electrons that condense on the solid electrode ($0 \le \gamma \le 1$)

$\lambda = \dfrac{L}{C(T_m)(T_m - T_c)}$ — Second Kutateladze number

$\xi = \dfrac{x}{s(t)}$ — Transformed coordinate

$\rho(T)$ — Density of electrode

ρ^ℓ — Density of the liquid in the drop

$\tau = \dfrac{t\,\alpha(T_m)}{\ell_0^2}$ — Fourier number

σ — Laplace variable

ϕ — Work function of electrode

ψ — Phase of the response in s

$\omega = \dfrac{\ell_0^2}{\alpha(T_m)} f$ — Dimensionless excitation frequency

Appendix

Assuming that the drop has a uniform temperature distribution, and neglecting other losses (radiation), the rate of heat transfer to the drop can be written (Ref. 11)

$$-Q_m + (1-\gamma)V_c I + \int_{V_d} r_d J_D^2 dV - \frac{D}{Dt}\left(C_p V_D (T_D - T_m)\right) = 0 \quad \text{(A1)}$$

where

$$V_c = \phi + V_A + \frac{3}{2}\frac{kT_e}{e}. \quad \text{(A2)}$$

If the rate of droplet formation is assumed to be steady-state and the average droplet geometry is used, Kim showed (Ref. 11, p. 155) that

$$Q_m \approx \frac{A\,V_s \rho^\ell J_D^2\, t_D}{3} + \frac{V_c(1-\gamma)\,I}{2}. \quad \text{(A3)}$$

For a droplet radius on the order of the electrode diameter (spray transfer), the Joule heating is several orders of magnitude less than the contribution from electron condensation. Q_m is finally approximated by

$$Q_m = \frac{V_c(1-\gamma)\,I}{2}. \quad \text{(A4)}$$

Note that the model will be most effective for spray transfer. Equation 3 can now be written as

$$-K(T)\frac{\partial T}{\partial Z} + V_c J(t)\left(\frac{\gamma+1}{2}\right) = \rho(T) L\left(V_z(t) - \frac{d\ell}{dt}\right). \quad \text{(A5)}$$

Equation 1 can be made dimensionless in the form of

$$\frac{\partial^2 v(u)}{\partial x^2} + q_j(\tau) r^*(u) = C(u)\left(W(\tau)\frac{\partial v(u)}{\partial x} + \frac{\partial v(u)}{\partial \tau}\right) \quad \text{(A6)}$$

with dimensionless boundary conditions

$$v(x=0,\tau)=0,$$
$$v(x=s(\tau),\tau)=v_m,$$
$$-\frac{\partial v}{\partial x}+\left(F\,q_j(\tau)\right)^{\frac{1}{2}}=\lambda\left(W(\tau)\frac{ds}{d\tau}\right) \quad \text{(A7)}$$

and dimensionless initial conditions

$$s(\tau=0)=1,$$
$$v(x,\tau=o)=v_o(x) \quad \text{(A8)}$$

The governing equation for steady-state can be by found by setting the time derivatives in Equations A6 to A8 to zero and changing the partial derivatives with respect to x to ordinary derivatives:

$$\frac{d^2v(u)}{dx^2}+q_jr^*(u)=C(u)W\frac{dv(u)}{dx} \quad \text{(A9)}$$

Here the boundary is fixed at s = 1, giving the boundary conditions

$$v(x=o)=0,$$
$$v(x=1)=v_m \quad \text{(A10)}$$

The problem is subject to the auxiliary condition that enough energy must be supplied at x = 1 that the electrode undergoes a phase change:

$$-\frac{dv}{dx}+\left(Fq_j\right)^{\frac{1}{2}}=\lambda W \quad \text{(A11)}$$

Equation A11 determines the q_j (the welding current) for which the solutions of Equations A9 and A10 are valid.

The steady-state Equations A9 to A11 are treated like an eigen value problem (Ref. 18) with Equation A9 rewritten as two first order equations by letting

$$y_1=\frac{dv}{dx},$$
$$y_2=v$$
$$y_3=q_j \quad \text{(A12)}$$

which gives

$$\frac{dy_1}{dx}=-y_3r^*(u)+C(u)W\,y_1$$
$$\frac{dy_2}{dx}=y_1$$
$$\frac{dy_3}{dx}=0 \quad \text{(A13)}$$

The boundary conditions for Equation A13 are

$$y_2(0)=0$$
$$y_2(1)=v_m$$
$$-y_1=-\left(F\,y_3\right)^{\frac{1}{2}}+\lambda W \quad \text{(A14)}$$

A relaxation method is used to solve for y_1, y_2, and y_3 (Ref. 18). The steady-state model predicts q_j given W,

$$q_j=q_j(W)=q_j\left(\frac{\ell_{ss}v_z}{T_m}\right).$$

The steady-state EE, is given from

$$\frac{I^2\ell_{ss}^2\,r(T_m)}{A^2K(T_m)(T_m-T_c)}+q_j\left(\frac{\ell_{ss}v_z}{T_m}\right)=0 \quad \text{(A15)}$$

given the material constants, the welding current I, the electrode feed speed v_z, and $q_j(W)$.

The transient problem, Equations A6 to A8, is solved by using the coordinate transformation

$$\xi(\tau)=\frac{x}{s(\tau)} \quad \text{(A16)}$$

to fix the moving boundary according to (Ref. 10). The resulting nonlinear partial differential equation is solved by using central differences in ξ for unequally spaced nodes (Ref. 19). The nodes are spaced in a geometric progression with more nodes near the ξ = 1 boundary. A backward differentiation method for stiff equations is used to solve the resulting set of ordinary differential equations.

To calculate v, K(T) is first smoothed from room temperature to the melting point using a moving average to avoid step changes in K(T) when the material changes from one solid phase to another; a piecewise cubic spline is then fit to the tabulated K(T) and integrated. Tabulated values of α(T) and r(T) are then written as functions of v, smoothed and fitted with piecewise cubic splines.